Surface Brillouin light spectroscopy of high-frequency guided elastic waves in CoFeB-multilayers on lithium niobate

Fehima Ugarak [1], Léa La Spina [1], Aurélie Solignac [2], Quentin Micard [1], Alexis Mosset [1], Samuel Margueron [1], Ausrine Bartasyte [1], Thibaut Devolder [3], and Vincent Laude [1]

[1] Université Marie et Louis Pasteur, SUPMICROTECH, CNRS, institut FEMTO-ST; 25000 Besançon, France

[2] Université Paris-Saclay, CEA, CNRS, SPEC, 91191 Gif-sur-Yvette, France

[3] Université Paris-Saclay, CNRS, Centre de Nanosciences et de Nanotechnologies, 91120 Palaiseau, France

E-mail: `vincent.laude@femto-st.fr`

Abstract. CoFeB alloy is a ferromagnetic material that is often considered to produce synthetic antiferromagnets (SAF) used in spintronic devices. SAF host spin waves with high tunability, making their coupling with surface acoustic waves (SAW) a promising avenue for next-generation communication devices. This coupling offers potential advantages such as SAW tunability and non-reciprocal operation in the multi-gigahertz range. Epitaxial lithium niobate (LN) thin films on sapphire substrates have emerged as a promising solution for achieving high SAW phase velocities. The combination of LN thin films with SAF, for instance based on CoFeB-based multilayers, hence offers new possibilities for engineering acoustic wave propagation. As the elastic properties of CoFeB depend on the composition of the alloy, their determination is a requisite to evaluate SAW dispersion. We investigate elastic wave dispersion in $Co_{40}Fe_{40}B_{20}$-based multilayers on LN/ZX-sapphire, ZX-LN, and SiO_2/Si substrates, combining surface Brillouin light spectroscopy and finite element computations. Surface-guided phonons ranging from 9 to 18 GHz are observed, for a wavelength of about 300 nm, and the elastic constants of $Co_{40}Fe_{40}B_{20}$ are estimated from them.

Keywords: synthetic antiferromagnets, surface acoustic waves, surface Brillouin light spectroscopy, CoFeB multilayers

Submitted to: *J. Phys. D: Appl. Phys.*

1. Introduction

Surface acoustic wave technology is traditionally based on metallic interdigital transducers (IDTs) deposited on a piezoelectric substrate. IDTs are defined by a two-dimensional lithography mask that includes periodic repetitions of interleaved electrodes, or fingers, the spatial periodicity of which imposes the SAW wavelength at resonance [1]. The lateral resolution of deep-UV lithography, used to transfer the mask as a pattern of electrodes, then typically limits the operation frequency of SAW filters to a maximum of about 3.7 GHz on single-crystal piezoelectric substrates such as lithium niobate (LN). Surpassing this frequency limit is a highly desirable advancement [2]. One possibility is to use free-standing piezoelectric thin films to prepare bulk acoustic wave resonant (BAR) filters, at the expense of additional delicate technological steps. Furthermore, BAR filters rely on resonant standing waves rather than on wave propagation as in the case of SAW filters, with implications of the filtering functions that can be achieved. Since the frequency limit is set by the phase velocity of SAW, another approach is to use a piezoelectric thin films (e.g. of LN) on top of a high-velocity substrate such as sapphire (Al_2O_3). For the same interdigital transducer mask, the operation frequency would then be around 5 GHz for LN on sapphire as compared to 3.7 GHz for a LN substrate. There is furthermore a strong interest in making SAW devices tunable or non reciprocal. This can be achieved through coupling with spin waves, e.g. in synthetic antiferromagnets (SAF) [3]. One possibility to realize a SAF is the deposition of nanometric multilayers of two or more ferromagnetic CoFeB alloy layers separated by metal spacers. The presence of additional layers, that are normally not used in SAW devices, has however an obvious direct influence on SAW velocity and even on the existence of certain modes of propagation in the multilayer considered as a whole. Hence a precise characterization of elastic constants is necessary. The elastic constants of CoFeB, for instance, are still under investigation [4, 5] and furthermore depend on the composition of the alloy.

In this work, we consider a series of samples combining thin layers of CoFeB ($Co_{40}Fe_{40}B_{20}$) alloy, tantalum (Ta), and ruthenium (Ru), deposited on substrates composed of either a thick layer of silicon oxide on silicon, (001)LN, or a (001)LN thin-film grown epitaxially on (001)sapphire. These combinations, although they do not constitute a complete SAF, offer the opportunity to check the elastic constants of the various materials, but also the dispersion and surface localization of various surface guided waves. Specifically, the velocity and dispersion of high-frequency elastic waves guided in the multilayers are obtained experimentally by surface Brillouin light spectroscopy (SBLS). They are compared to numerical simulations based on a finite element model (FEM) taking into account radiation inside the substrate through the use of a perfectly matched layer (PML) and accounting for piezoelectricity. High-frequency guided elastic waves in this work are observed in the range from 5 to 20 GHz. Their polarization is generally of the hybrid type, involving a combination of all three displacements in space. They include Rayleigh, Love and Sezawa-type surface

Table 1. Multilayer samples studied in this work, with numbers in parentheses indicating the thickness of each layer (units of nm). The first material indicated in each case is the substrate. LN: lithium niobate.

Sample	Multilayer
A	$Si/SiO_2(500)//Ta(6)/Ta(26)/Ru(0.44)/Ta(4)$
B1	$Si/SiO_2(500)//Ta(6)/CoFeB(100)/Ru(0.44)/Ta(4)$
B2	$Si/SiO_2(500)//Ta(6)/CoFeB(100)/Ru(0.44)/Ta(8)$
B3	$Si/SiO_2(500)//Ta(6)/CoFeB(50)/Ru(0.44)/Ta(4)$
B4	$Si/SiO_2(500)//Ta(6)/CoFeB(26)/Ru(0.44)/Ta(4)$
C	$LN//Ta(3)/CoFeB(60)/Ru(0.4)/Ta(3)$
D	$Al_2O_3/LN(110)//Ta(3)/CoFeB(60)/Ru(0.4)/Ta(3)$

waves, but also leaky surface waves of shear or longitudinal character. The results confirm that metallic multilayered stacks on thin film of LN on sapphire are promising candidates for high-frequency SAW devices.

2. Methods

In this section we first introduce the multilayer samples and their techniques of elaboration, then we describe SBLS measurements, and finally we present FEM computations for obtaining the dispersion of surface guided elastic waves.

2.1. Samples preparation

A total of seven different samples (as detailed in table 1) were deposited by sputtering using a Rotaris-Singulus system, in a chamber with a base pressure of 1×10^{-7} mbar. The deposition process was carried out under an argon pressure of 5×10^{-3} mbar. The layer thicknesses were verified using X-ray reflectivity (XRR). Ta buffer and Ru/Ta capping layers were employed for their smoothing properties and were selected based on optimized SAF structures reported in [6]. The metallic layers of Ta and Ru are supposed to be amorphous and hence elastically isotropic. The ferromagnetic layer of CoFeB is usually also considered amorphous and elastically isotropic in the literature [7]. The choice of CoFeB thickness in the different samples, from 26 to 100 nm is here made so that it has a definite influence of the phase velocity of surface waves and hence allows us to estimate the elastic properties of the deposited material, here alloy $Co_{40}Fe_{40}B_{20}$. In an actual SAF, the CoFeB thickness would be slightly smaller, of the order of 10 nm, and the influence on SAW dispersion would correspondingly be slightly less.

Three different substrates were considered. Samples A, B1, B2, B3, and B4 all involve a thick layer of 500 nm amorphous thermal silicon oxide on a substrate of (100) silicon wafer. The thickness of silicon oxide is chosen to be large to minimize the influence of the silicon substrate on the dispersion of high-frequency guided elastic waves. The difference between sample A and other samples is the absence of the CoFeB layer which has been replaced by a Ta layer with similar thickness as CoFeB in sample B4.

The LN substrate (provider: Roditi) of sample C is oriented so that crystallographic axis Z is orthogonal to the surface (z reference axis in figure 1) and crystallographic axis X is aligned with reference axis x.

Sample D is elaborated on a sapphire substrate covered with an epitaxial piezoelectric layer of LN. Epitaxy techniques, where material is directly deposited on a substrate, allow us to achieve thicknesses below 300 nm. In our case metal-organic chemical vapor deposition (MOCVD) was used [8]. A high-quality epitaxial LN film with pure LN phase and controlled non-stoichiometry was produced by pulsed injection MOCVD. A Z-oriented LN (Z-LN) layer can be obtained by using a C sapphire substrate. LN deposition on C sapphire was performed for 4 h at evaporation and deposition temperatures of 265°C and 750°C, and a pressure of 9.33 mbar. The Li:Nb molar ratio was 1.17. X-ray diffraction (XRD) measurement showed the (0006) and (00012) reflections corresponding to the Z orientation and the presence of a reflection at about 54.6° that could correspond to the (410) reflection of the Li-poor phase ($LiNb_3O_8$) or (211) of the LN. We confirmed, with Raman spectroscopy measurements, that the layer does not present any parasitic phase. Furthermore, the composition of the layer, although estimated to be subcongruent (between 48.1 and 48.3 mol% of Li_2O), is homogeneous over the wafer. Finally, ellipsometry and focused ion beam (FIB) measurements allowed us to determine that the deposited layer had a thickness of approximately 110 nm and that the surface had a roughness of approximately 1.6 nm.

2.2. Surface Brillouin light spectroscopy

Experimental studies are performed with the SBLS technique. The experimental geometry is depicted in figure 1. SBLS is extensively employed to investigate the physical properties of thin films [9, 10, 11, 12], interfaces [13, 14], and layered materials [9, 15, 14]. It is essential for determining the elastic properties of materials that are opaque or nearly opaque, such as metallic layers. The significant optical absorption restricts the laser penetration depth, confining the measurement very close to the surface. Metals exhibit high absorption at visible wavelengths, indeed, resulting in a penetration depth of the order of a few nanometers to tens of nanometers [16].

SBLS measurements were conducted in the backscattering configuration shown in figure 1, with a 200 mW linearly polarized laser operating at a wavelength $\lambda_0 = 532$ nm. Measurements were performed with an angle of incidence ϕ varying in the range from 40° to 80°. Measurements further allow for the phonon propagation angle ψ to vary from 0° (along the x-axis) to 90° (along the y-axis), by rotating the sample in-plane.

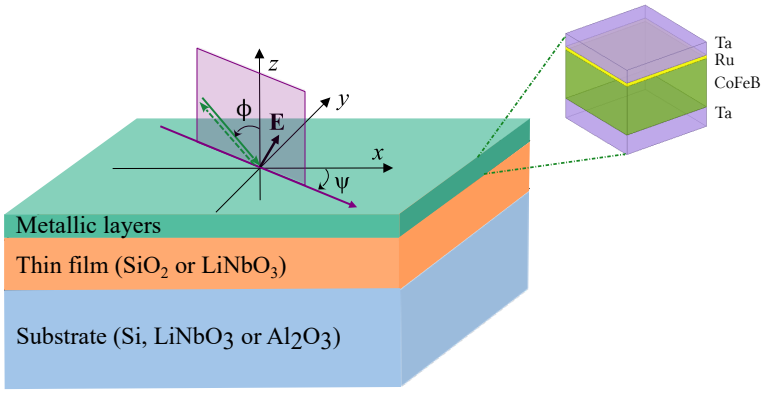

Figure 1. Experimental configuration. The metallic stacks of Ta/CoFeB/Ru/Ta (see inset) were deposited on Si/SiO_2 (500 nm), on Z-LN, or on Z-sapphire/Z-LN (110 nm), as substrates. The orthogonal reference frame (x, y, z) is used both as a reference frame for numerical simulation and as an experimental reference frame. With respect to the hexagonal crystallographic reference frame (case of LN and sapphire), axis z is parallel to the c-axis and axis x is parallel to the a-axis. ϕ is the angle of incidence of the laser beam in the surface BLS experiment, and ψ is the in-plane angle of the phonon wave vector. Incident and backscattered optical wave vectors are figured with solid green and dashed green arrows, respectively.

Surface phonons with an in-plane wavenumber $q = 2k \sin\phi$ (with $k = 2\pi/\lambda_0$ being the optical wavenumber) contribute to light scattering, producing Brillouin peaks with Lorentzian profiles centered at frequency shift f, whereas the peak width reflects the phonon lifetime (not used here). The surface phonon phase velocity v is related to the frequency shift by relation $v = \lambda_0 f/(2\sin\phi)$. Note that the phase velocity v also explicitly depends on angle ψ.

Backscattered light was analyzed using a six-pass tandem Fabry-Pérot interferometer (TFP-2 HC, The Table Stable LTD) with a mirror spacing of either 8 mm or 4 mm and a scanning amplitude of 450 nm. Brillouin frequency shifts were extracted using a homemade written Matlab code, employing multi-Lorentzian curve fitting. Dynamical surface corrugation (the ripple effect) leads to inelastic light scattering, which is effective only for the normal component $u_z = u_3$ of the phonon displacement field. Laser light, polarized in the incidence plane (p-pol), thus enhances the ripple effect for sagittally polarized SAWs [16]. In the measurements, we used a collection lens with a numerical aperture of ≈ 0.1. The limited aperture affects the precision of SAW velocity and attenuation measurements [17]. The numerical aperture that was chosen corresponds to a trade-off between precision and acquisition time.

2.3. Guided elastic wave dispersion

For interpretation of experimental results, we compare them to the dispersion relation of elastic waves guided in the multilayers. For this purpose we use a method [18, 19, 20] for mapping wave dispersion from the response of the structure to a spatially random excitation applied to the top layer, including radiation loss. The numerical

implementation combines a perfectly matched layer (PML) with finite element analysis. The multilayer is represented by a one-dimensional mesh that describes the precise geometry of the multilayer along the depth. The piezoelastic equations are solved while imposing the surface phonon wavenumber along a given propagation direction. The response is specifically computed as the square of the vertical displacement $|u_3|^2$, following the theory of the ripple effect [21]. In this way, numerical computations can be directly compared to surface BLS experiments. A summary of the important implementation details is given in Appendix A.

Table 2. Elastic constants and mass density for CoFeB alloy.

	This Work	**Reference** [4]	**Reference** [5]	**Reference** [22]
	$Co_{40}Fe_{40}B_{20}$	$Co_{20}Fe_{60}B_{20}$	$Co_{20}Fe_{60}B_{20}$	$Co_{20}Fe_{60}B_{20}$
Elastic Constants (GPa)				
c_{11}	180	283	210	250
c_{12}	70	165	130	100
c_{44}	55	59	45	75
Density (kg/m^3)				
ρ	7 800 [23]	–	6 970 [22]	6 970

Since the primary objective of this study is to investigate the dispersion of elastic waves in multilayered CoFeB-based structures deposited on Si/SiO_2, on LN, and on sapphire/LN, we need material constants for all materials. The elastic constants of silicon (with cubic symmetry) are taken from [24] and the elastic constants of silicon oxide (with isotropic symmetry) from [25]. For the trigonal symmetry substrates, elastic and piezoelectric constants of lithium niobate are taken from [26] and elastic constants of sapphire from [27]. Mass densities are given in the above references. Ta is considered isotropic, with elastic constants $c_{11} = 265$ GPa and $c_{12} = 158.6$ GPa [28] (at room temperature), and mass density $\rho = 16600$ kg/m^3. Ru is also considered isotropic, with elastic constants $c_{11} = 601.7$ GPa and $c_{12} = 257.9$ GPa, calculated from Young's modulus $E = 447$ GPa and shear modulus $G = 173$ GPa [29], for a Poisson's ratio of 0.3. The mass density for Ru is $\rho = 12450$ kg/m^3. CoFeB is considered amorphous and hence elastically isotropic. Several sets of quite different material constants can be found in the literature for alloy $Co_{20}Fe_{60}B_{20}$ [4, 5, 22], as listed in table 2. As discussed below, we adjusted the elastic constants for alloy $Co_{40}Fe_{40}B_{20}$ to match numerical simulations with BLS measurements. The mass density of $Co_{40}Fe_{40}B_{20}$ is taken as $\rho = 7800$ kg/m^3 [23].

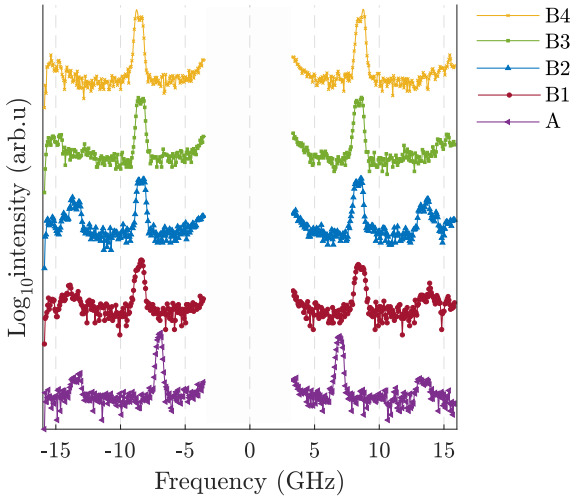

Figure 2. Spectra of BLS measurements performed on A, B1, B2, B3 and B4 samples (described in table 1). The angle of incidence is $\phi = 70°$.

3. Results

The propagation of SAW on opaque or semi-opaque materials creates periodic displacements on the surface, also known as ripple-like structures, providing information about SAW that is conveyed by the scattered light [16, 30]. In homogeneous materials, the Rayleigh wave phase velocity is dispersionless [31, 32] and less than the smallest bulk shear wave velocity. Dispersion is in contrast the rule in multilayer thin films. The measurement of surface phonon dispersion can be used to estimate the relevant material properties by comparison with a numerical model. We present in the following the SBLS measurements we conducted on the various samples listed in table 1.

3.1. Samples A and B1-B4

We conducted SBLS measurements in the backscattering configuration with a $\phi = 70°$ angle of incidence for samples A, B1 - B4 (see table 1 for the composition). For all those samples, the substrate is Si/SiO_2(500 nm). We assume that the elastic constants of silicon and amorphous silicon oxide are known precisely. The main goal is then to assess the accuracy with which the elastic constants for tantalum (Ta), ruthenium (Ru), and CoFeB alloy are known. Surface Brillouin spectra are given in figure 2.

Two main peaks are observed, corresponding to a Rayleigh-type surface acoustic wave (RW) and a Sezawa wave (SW). For samples of type B, the RW peak intensity seems inversely proportional to the CoFeB layer thickness, likely due to increasing roughness.

Table 3 compares experimental peak frequencies for the Rayleigh and the Sezawa waves with the FEM simulation. Experimental uncertainties are estimated by fitting both Stokes and anti-Stokes spectra to Lorentzian profiles. The measurement resolution is estimated to be 0.062 GHz (total scan amplitude of 31.7 GHz over 512 measurement

Table 3. Frequency shifts of the Rayleigh wave (RW) and the Sezawa wave (SW) obtained via FEM simulation and BLS experiment in figure 2.

Sample	BLS Experiment (GHz)		FEM Simulation (GHz)	
	RW	SW	RW	SW
A	6.95 ± 0.03	13.38 ± 0.04	7.05	12.26
B1	8.45 ± 0.03	13.91 ± 0.04	8.20	13.93
B2	8.42 ± 0.03	13.65 ± 0.04	8.03	13.64
B3	8.47 ± 0.03	15.09 ± 0.06	8.18	14.75
B4	8.72 ± 0.03	15.32 ± 0.06	8.50	14.97

channels). Full widths at half-maximum (FWHM) are ~ 0.6 GHz for RW peaks and ~ 1.3 GHz for SW peaks.

Sample A does not contain a CoFeB layer and is dominated by Ta rather than Ru in terms of thickness. The simulated frequency shifts show reasonable agreement with the experimental ones, suggesting that the literature values for the elastic constants of Ta and Ru are reasonably appropriate. Indeed, given the small thickness of these layers, we infer that their influence on the propagation of surface acoustic waves is either negligible or not dominant for the other samples.

Samples B1 and B2 both feature a 100 nm CoFeB layer, with the distinction lying in the top Ta layer, which is 4 nm thick for sample B1 and 8 nm thick for sample B2. This variation allows for the assessment of the influence of the Ta thickness on Brillouin frequency shifts.

The thickness of the CoFeB layer is then varied across 100, 50, and 26 nm for samples B1, B3 and B4; respectively. This thickness has an influence on the dispersion of the Rayleigh and more notably the Sezawa waves. Overall, the match between experimental and computed frequency shifts is fair. As a note, of the different material constants sets for CoFeB listed in table 2, Gueye et al.'s [4] values match experiments equally well as ours for samples B1-B4, though using mass density from [23]; the two other sets definitely do not. The Rayleigh frequency is mostly influenced by the value of c_{44}, whereas the Sezawa frequency is mildly sensitive to the value of c_{11} ($c_{12} = c_{11} - 2c_{44}$ per the assumption of isotropy for CoFeB). These two values were adjusted to fit with the experimental Brillouin frequency shifts. As such, however, the two SBLS frequencies available for each B-type sample are not enough to fully determine precisely c_{11} and c_{44}, and the final values in table 2 also take into account the results with samples C and D reported subsequently; with those samples taken into account, Gueye et al.'s values [4] do not match anymore our experiments.

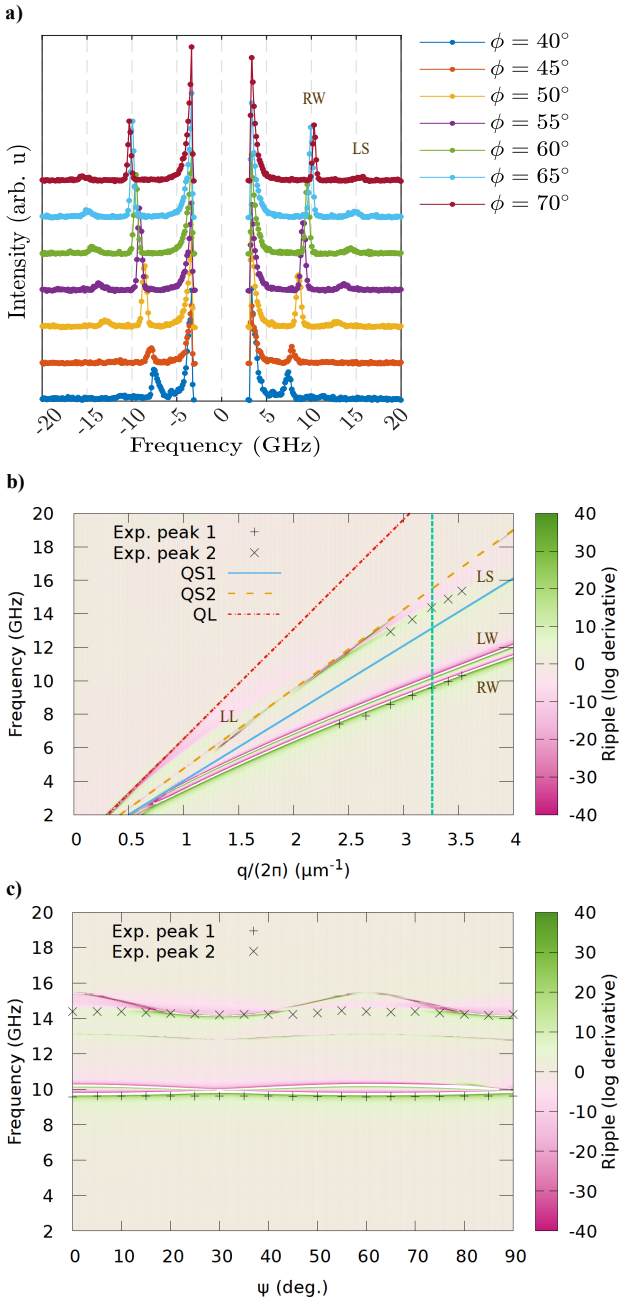

Figure 3. Sample C. (a) Surface BLS spectra of the Ta/CoFeB/Ru/Ta stack on a LN(001) substrate are measured for different angles of incidence ϕ, for in-plane angle $\psi = 0°$. (b) Surface phonon dispersion is computed for frequency as a function of wavenumber $q/(2\pi)$, for $\psi = 0°$. The quasi shear (QS) quasi longitudinal (QL) bulk waves of the substrate are shown. (c) The in-plane dispersion is shown at the fixed wavenumber $q/(2\pi) = 3.26$ μm^{-1} or $\phi = 60°$ (green vertical line in panel (b)). Angles $\psi = 0°$ and $\psi = 90°$ correspond to propagation along the x and y axes respectively. In panels (b) and (c), crosses represent surface BLS measurements and the color bars represent the logarithmic derivative of the ripple response.

3.2. Sample C

Sample C is deposited on a LN substrate with the [001] direction aligned with axis z. Angles are measured in-plane with respect to the X axis or [100] direction. Surface Brillouin spectra obtained by varying the angle of incidence are shown in figure 3(a). Two peaks can be distinguished in both Stokes and anti-Stokes spectra which are verified to be symmetric. As a note, the signal for frequency shifts $|f| < 5$ GHz is the pedestal of the elastic (Rayleigh) scattering peak that is filtered by the tandem Fabry-Pérot interferometer. The experimental surface phonon wavevector $q = 4\pi/\lambda_0 \sin\theta$ is varied thanks to the angle of incidence, for the fixed optical wavelength λ_0. An observed frequency f is related to a phonon propagating along the surface at phase velocity v by $f = vq/2\pi$. figure 3(b) shows the dispersion map for surface elastic waves computed using the technique described in Section 2.3. The color map accounts for the logarithmic derivative of the ripple response; surface wave solutions are located along the transitions from positive to negative values, where the logarithmic derivative goes through zero. The linear dispersion of the bulk acoustic phonons of the substrate have been added as a guide for the eye. Surface waves appearing below the slowest quasi-shear phonon (QS1) are true surface waves; those appearing above are in principle leaky surface waves. An in-plane dispersion map is further shown in figure 3(c) as a function of the in-plane angle ψ, at a fixed wavenumber ($q/2\pi = 3.26$ µm^{-1}, $\phi = 60°$).

The layered structure theoretically allows for the propagation of 4 surface modes, annotated Rayleigh wave (RW), Love wave (LW), leaky SAW (LS) and longitudinal leaky SAW (LL) in figure 3(b). Among those 4 modes, only 2 are observed experimentally, RW and LS. The dispersion of the Rayleigh wave aligns well with the numerical simulation. Its identification is based on its lower velocity and pronounced dominance in (p-p) polarized BLS measurements. The distribution of displacements for this wave, depicted in figure 4(a), confirms its generalized Rayleigh character and the dominance of vertical displacement u_3 at the surface. In general, the depolarized scattering (p-s) caused by Love waves of pure shear polarization is expected to be weak [9]. The non-appearance of the LW in the experiment may be consistent with this argument. As figure 4(b) shows, however, the distribution of displacements for this wave is dominated by the shear component u_2 but the vertical component u_3 does not vanish at the surface. The small frequency difference between RW and LW in comparison to the Brillouin peak widths may, however, be the reason why they are not distinguished in experiment. The dispersion of the leaky SAW extends in between the two shear elastic waves of the substrate. This wave gives a small but identifiable Brillouin signal that conforms with the numerical simulation. Finally, the longitudinal leaky SAW appears in between the fast shear and the longitudinal elastic waves of the substrate, but does not leave a trace in the Brillouin spectra for $q/2\pi > 2$ µm^{-1}.

Anisotropy in the plane for a fixed angle of incidence ($\phi = 60°$) can be evaluated from figure 3(c). The frequency shifts for the RW and the LS vary only slightly with angle ψ, in agreement with the numerical simulation. They are approximately 9.5 GHz

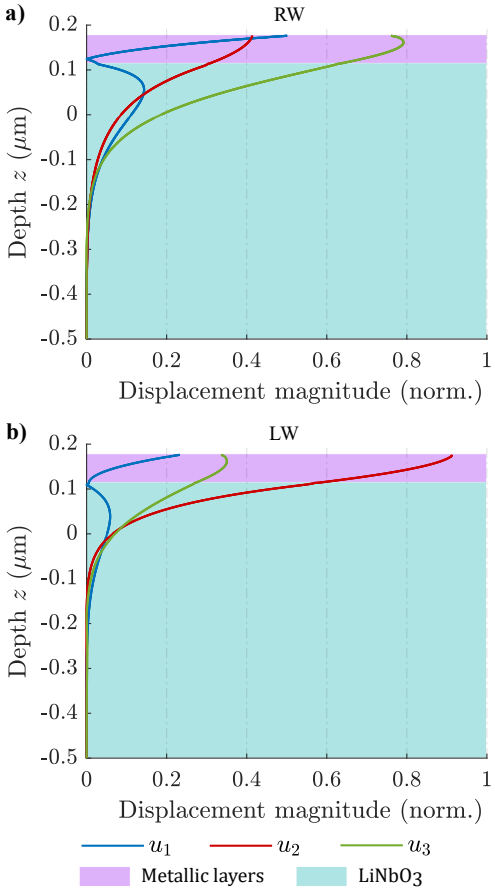

Figure 4. Modulus of the displacements in the depth for (a) the Rayleigh wave (RW) and (b) the Love wave (LW) of sample C, at angle of incidence $\phi = 60°$.

for the RW and 14.3 GHz for the LS. As a note, anisotropy of surface phonons is here only induced by the anisotropy of the substrate since the layers are assumed isotropic.

3.3. Sample D

Sample D is formed of the same sequence of layers deposited on a LN thin-film on a sapphire substrate with the [001] direction oriented along axis z. Angles are again measured in-plane with respect to the X axis or [100] direction. The thickness of the LN layer was first estimated by ellipsometry, then confirmed on a piece in the center of the wafer by a vertical FIB sectioning of the film. With these characterizations, we determined a thickness of around 110 nm, with a roughness of around 2 nm.

Surface Brillouin spectra obtained by varying the angle of incidence are shown in figure 5(a). Two peaks can be distinguished in Stokes and anti-Stokes spectra, as for sample C, but the peak highest in frequency is better resolved. Figure 5(b) shows the dispersion map for surface elastic waves computed using the technique described in Section 2.3. As in figure 3, the color map accounts for the logarithmic derivative of the ripple response; surface wave solutions are located along the transitions from

positive to negative values, where the logarithmic derivative goes through zero. The linear dispersion of the bulk acoustic phonons of the substrate have been added as a guide for the eye. Surface waves appearing below the slowest quasi-shear phonon (QS1) are true surface waves; those appearing above are in principle leaky surface waves. An in-plane dispersion map is further shown in figure 5(c) as a function of the in-plane angle ψ, at a fixed wavenumber ($q/2\pi = 3.41$ µm^{-1}, $\phi = 65°$).

In figure 5(b), six distinct waves are identified and denoted Rayleigh wave (RW), Love wave (LW), Sezawa wave (SW), higher-order surface waves (SW2 and SW3), and leaky longitudinal SAW (LL). The first 5 are guided surface waves, whereas the last is a leaky surface wave. Among those 6 waves, only 2 are observed experimentally. The Rayleigh wave and the Love wave are rather similar to the case of sample C in terms of frequency dispersion. The displacements displayed in figure 6(a,b) confirm this observation. The Sezawa wave, that was not observed with sample C, now gives a Brillouin signal, whereas the LS of sample C is not present. The displacements plotted in figure 6(c) confirm that the SW is mostly polarized in the sagittal plane. The higher-order surface waves SW2 and SW3 are dominantly polarized in the plane of the surface, in contrast to the Sezawa wave, as figure 6(d,e) shows.

All waves exhibit a nonzero u_3 displacement component at the surface, that could produce a ripple signal. This component, however, is most significant for the RW and the SW, consistently with experimental observation. Whereas the ripple signal should be small for the SW2 and the SW3, this may not be the case for the LW. The small frequency difference between RW and LW may, however, make them indistinguishable given the Brillouin peak widths.

Anisotropy in the plane for a fixed angle of incidence ($\phi = 65°$) can be evaluated from figure 5(c). The frequencies for the RW and the SW vary only slightly with angle ψ, in agreement with the numerical simulation. They are approximately 10.5 GHz for the RW and 15.7 GHz for the SW. As a note, anisotropy of surface phonons is here only induced by the anisotropy of the substrate and the LN layer, since the layers are assumed isotropic.

4. Discussion

The experimental surface BLS peaks that have been obtained with all samples in this study are of a better quality than in the case of a bare LN on sapphire sample [19] (in terms of fidelity to the Lorentzian shape, peak width, and peak intensity), though they were all acquired with the same experimental apparatus and under equivalent conditions. This fact does not seem to be correlated to surface roughness but rather to the metallic character of the SAF multilayers that enhances the ripple signal.

The agreement between numerical and experimental dispersion of the observed surface waves is quite good overall and significantly better than the previous agreement with a bare LN on sapphire sample. Since the numerical simulation technique is the same, we attribute this progress to the enhanced experimental data quality quoted

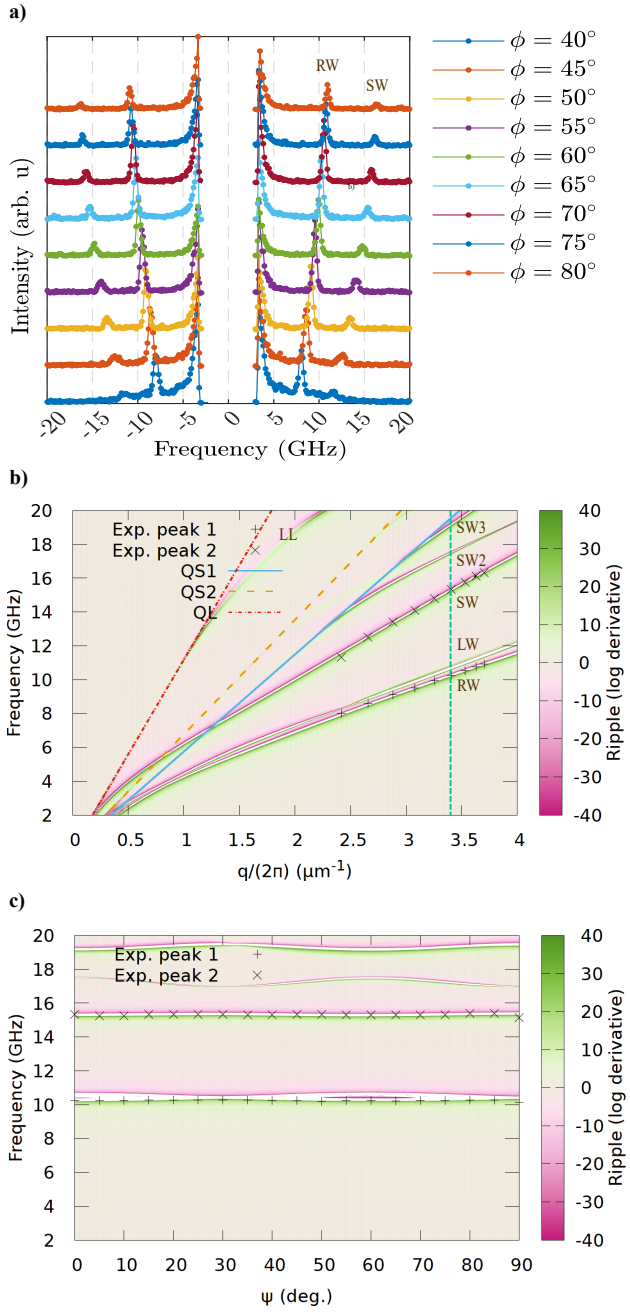

Figure 5. Sample D. (a) Surface BLS spectra of the Ta/CoFeB/Ru/Ta stack on a LN(001) thin-film on a sapphire substrate are measured for different angles of incidence ϕ, for in-plane angle $\psi = 0°$. (b) Surface phonon dispersion is computed for frequency as a function of wavenumber $q/(2\pi)$, for $\psi = 0°$. The quasi shear (QS) quasi longitudinal (QL) bulk waves of the substrate are shown. (c) The in-plane dispersion is shown at the fixed wavenumber $q/(2\pi) = 3.41$ μm^{-1} or $\phi = 65°$ (green vertical line in panel (b)). Angles $\psi = 0°$ and $\psi = 90°$ correspond to propagation along the x and y axes respectively. In panels (b) and (c), crosses represent surface BLS measurements and the colorbars represent the logarithmic derivative of the ripple response.

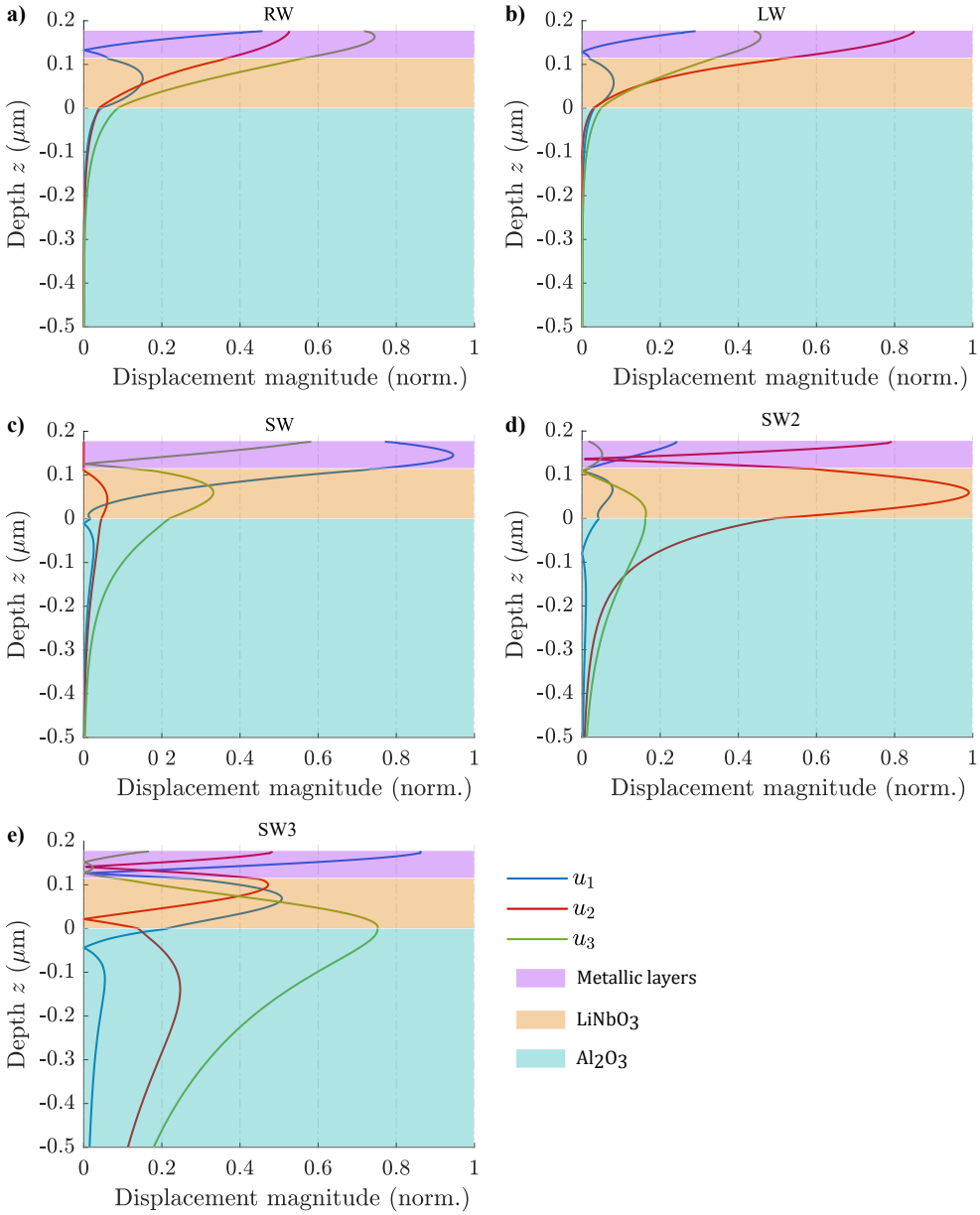

Figure 6. Modulus of the displacements in the depth for (a) the Rayleigh wave (RW), (b) the Love wave (LW), (c) the Sezawa wave (SW), and (d-e) the higher-order surface waves SW2 and SW3 of sample D, at angle of incidence $\phi = 65°$.

above. This agreement was obtained without adjusting the elastic constants of the substrate materials (silicon, silicon dioxide, lithium niobate, and sapphire), nor of the Ta and Ru layers, but the two independent elastic constants of CoFeB alloy. We adjusted very slightly the value of c_{44} compared to the literature (see table 2) but in a larger extent the value of c_{11}. This adjustment is key in the agreement between numerical and experimental dispersion for both samples C and D. As a note, we verified that the agreement is degraded when using the elastic constants [4] in the third column of table 2. The results suggest that the elastic constants of CoFeB alloy depend quite strongly

Table 4. Comparison of surface wave frequencies for samples C and D, compared with the LN layer on sapphire case [19], for $q/2\pi = 3.5$ µm^{-1} obtained via FEM simulation.

Waves	C	D	ZX-sapphire// ZX-LN
RW	10.3 GHz	10.5 GHz	13.0 GHz
LW	10.8 GHz	10.9 GHz	14.5 GHz
SW	-	15.7 GHz	19.0 GHz
LS	15.0 GHz	-	-
LL	-	-	28.0 GHz

on the mixture of Co and Fe elements.

Table 4 lists some of the surface waves that were identified in samples based on LN. The comparison is thus between the SAF multilayer deposited on a LN substrate (sample C) or on a LN thin-film on sapphire (sample D); for the latter case a comparison with a similar substrate but without the SAF multilayer [19] is further useful. Both the Rayleigh wave (RW) and Love wave (LW) exist for all samples and have close frequencies. It appears the SAF multilayer slows down those surface waves significantly, presumably as a result of the mass-loading effect associated with the multilayer material. This may be interpreted as a downside of adding the SAF multilayer, since high frequency SAW operation is hindered. Note, however, that the thicknesses of CoFeB layers composing a SAF are generally smaller than those considered in this work, so the mass loading effect should be less pronounced.

Though the LW is not seen in surface BLS measurements, it can still be generated by means of IDTs on the piezoelectric surface and would induce displacements or strains quite different from those of the RW. This observation can have a direct influence on spin-phonon coupling in the SAF [33]. The Sezawa wave of sample D appears interesting for SAW applications since it appears at a higher frequency than the Rayleigh wave - about 15 GHz compared to about 10 GHz, depending on the phonon wavelength considered - while presenting clear surface confinement. A similar surface wave was previously observed without the SAF multilayer [19], at an even higher frequency, but the surface confinement seemed less efficient.

The leaky shear wave observed with sample C and the leaky longitudinal wave observed previously with a LN thin-film on sapphire sample [19] may be interesting due to their high frequency, but their leakage should be investigated before any conclusion is made.

5. Conclusion

The propagation of surface guided waves in CoFeB-based metal multilayers on a LN substrate or a thin LN film on sapphire was investigated. Numerical simulations

and experimental surface Brillouin light spectroscopy measurements revealed distinct dispersion characteristics for different substrate configurations. Key findings include the identification of four surface waves in the structure based on a LN substrate and six surface waves in the structure based on LN-on-sapphire. In both cases, only two of them were observed in surface Brillouin light spectra. Their dispersion and polarization were modelled using a finite element technique accounting for radiation of surface guided elastic waves in the semi-infinite substrate. We observed a general slowing down for all waves and an improved surface confinement for the Sezawa wave in the presence of a metal stack on ZX-LN on sapphire as compared to a bare ZX-LN/ZX-sapphire structure. The elastic constants for the CoFeB layer were adjusted as a result of matching SBLS measurements with the numerical dispersion. These insights advance the understanding of surface acoustic wave propagation in complex multilayer structures and have potential implications for high-frequency surface acoustic wave devices.

Acknowledgments

This work has been supported by the Agence Nationale de la Recherche (project MAXSAW, ANR-20-CE24-0025), the EIPHI Graduate School (Contract No. ANR-17-EURE-0002), and the Bourgogne-Franche-Comté Region. Support from the French Renatech network and its FEMTO-ST and C2N technological facilities is also gratefully acknowledged.

Appendix A. Computation of the ripple response

The elastodynamic equation describing time-harmonic elastic wave propagation is [19]

$$-\nabla.T - \rho\omega^2\mathbf{u} = \mathbf{f}, \tag{A.1}$$

with T the stress tensor, $\mathbf{u}$ the displacement vector, and $\mathbf{f}$ an applied body force. $\omega = 2\pi f$ is the angular frequency. Taking piezoelectricity into account, which must be done explicitly for LN, implies considering in addition Poisson's equation, describing the charge distribution

$$-\nabla.\mathbf{D} = 0, \tag{A.2}$$

with $\mathbf{D}$ the electric displacement vector. The constitutive relations of piezoelectricity are written

$$T_{ij} = c_{ijkl}S_{kl} + e_{kij}V_{,k}, \tag{A.3}$$

$$D_i = e_{ikl}S_{kl} - \epsilon_{ij}V_{,j}, \tag{A.4}$$

where c, e, ϵ and S are respectively the elastic, piezoelectric, dielectric and strain tensors and V is a scalar electric potential from which the electric vector derives. All vectors and tensors appearing above are then represented as finite element functions defined on the 1D mesh. Note that all fields include an implicit plane wave dependence $\exp(-\imath\mathbf{q}\cdot\mathbf{r})$

with **q** the phonon wavevector along the surface of the multilayer. Hence the strain components $S_{ij} = \frac{1}{2}(\frac{\partial u_i}{\partial x_j} - \imath q_j u_i + \frac{\partial u_j}{\partial x_i} - \imath q_i u_j)$, for instance.

The equations above are solved in weak form on a mesh using the finite element method [18]. The body force **f** is spatially random and applied only to the top metallic layers in this work. This way, we are favoring surface wave excitation from the surface, in accordance with the physics of surface BLS. The 1D mesh implements precisely the thickness of each layer in the vertical direction. The substrate, that is in principle semi-infinite, is replaced along the depth by 2 µm of the homogeneous substrate material, followed by 1 µm of a perfectly matched layer (PML) derived from it. The PML uses a smooth second-degree polynomial variation of the imaginary material constants [34] to avoid numerical reflection on the bottom PML border. Mechanical and electrical boundary conditions at the top surface are of the Neumann type, i.e. zero surface traction and no surface charges; at the PML bottom they are of the Dirichlet type (clamped boundary and vanishing potential).

Dispersion maps are produced by solving the governing equations for many (q, ω) points in the dispersion plane (in practice 100 wavenumbers by 2000 frequencies for panels (b) in Figures 3 and 5). Once the wave displacements have been obtained in the depth, the vertical displacement u_3 is used to estimate the ripple response as representative of surface BLS [20]. As a note, the logarithmic derivative of the ripple response [18] is defined as

$$\frac{\partial \log(|u_3|^2)}{\partial \omega} = \frac{1}{|u_3|^2} \frac{\partial |u_3|^2}{\partial \omega}. \tag{A.5}$$

That function makes the response almost independent of the applied excitation. Maxima of the ripple function $|u_3|^2$ are transformed into zeros of its logarithmic derivative.

References

[1] Hashimoto K 2000 *Surface acoustic wave devices in telecommunications* (Springer)

[2] Delsing P, Cleland A N, Schuetz M J, Knörzer J, Giedke G, Cirac J I, Srinivasan K, Wu M, Balram K C, Bäuerle C *et al.* 2019 *Journal of Physics D: Applied Physics* **52** 353001

[3] Verba R, Tiberkevich V and Slavin A 2019 *Physical Review Applied* **12** 054061

[4] Gueye M, Zighem F, Belmeguenai M, Gabor M S, Tiusan C and Faurie D 2016 *Journal of Physics D: Applied Physics* **49** 145003

[5] Shekhar S, Mielcarek S, Otani Y, Rana B and Trzaskowska A 2023 *Scientific Reports* **13** 10668

[6] Mouhoub A, Millo F, Chappert C, Kim J V, Létang J, Solignac A and Devolder T 2023 *Physical Review Materials* **7** 044404

[7] Seeger R L, Millo F, Mouhoub A, de Loubens G, Solignac A and Devolder T 2023 *Physical Review Materials* **7** 054409

[8] Almirall A, Oliveri S, Daniau W, Margueron S, Baron T, Boulet P, Ballandras S, Chamaly S and Bartasyte A 2019 *Applied Physics Letters* **114**

[9] Carlotti G 2018 *Applied Sciences* **8** 124

[10] Bassoli L, Nizzoli F and Sandercock J R 1986 *Physical Review B* **34** 1296

[11] Djemia P, Dugautier C, Chauveau T, Dogheche E, De Barros M I and Vandenbulcke L 2001 *Journal of Applied Physics* **90** 3771–3779

[12] Zerdali M, Hamzaoui S, Teherani F H and Rogers D 2006 *Materials Letters* **60** 504–508

[13] Jorna R, Visser D, Bortolani V and Nizzoli F 1989 *Journal of applied physics* **65** 718–725
[14] Beghi M G, Bottani C E, Ossi P M, Pastorelli R, Poli M, Tanner B K and Liu B X 1998 *Surface and Coatings Technology* **100** 324–328
[15] Beghi M, Bottani C E, Ossi P, Lafford T A, Tanner B K *et al.* 1997 *Journal of applied physics* **81** 672–678
[16] Mutti P, Bottani C E, Ghislotti G, Beghi M, Briggs G A D and Sandercock J R 1995 *Advances in acoustic microscopy* 249–300
[17] Elmiger M W 1988 *Raman scattering under high pressure in samariumselenide and Brillouin spectroscopy from surface acoustic waves* Ph.D. thesis ETH Zurich
[18] Laude V and Korotyaeva M E 2018 *Physical Review B* **97** 224110
[19] La Spina L, Micard Q, Mosset A, Margueron S, Bartasyte A and Laude V 2023 *Applied Physics Letters* **122**
[20] Ugarak F, Mosset A and Laude V 2024 *Applied Physics Letters* **125**
[21] Loudon R 1978 *Physical Review Letters* **40** 581
[22] Babu N K, Trzaskowska A, Graczyk P, Centała G, Mieszczak S, Głowiński H, Zdunek M, Mielcarek S and Kłos J W 2021 *Nano letters* **21** 946–951
[23] Kirk D, Kohn A, Borisenko K B, Lang C, Schmalhorst J, Reiss G and Cockayne D J H 2009 *Physical Review B—Condensed Matter and Materials Physics* **79** 014203
[24] Every A G, Sachse W, Kim K Y and Niu L 1991 *Review of Progress in Quantitative Nondestructive Evaluation: Volume 10B* 1663–1668
[25] Auld B A 1973 *Acoustic fields and waves in solids* (Ripol Klassik)
[26] Kovacs G, Anhorn M, Engan H E, Visintini G and Ruppel C C W 1990 Improved material constants for $LiNbO_3$ and $LiTaO_3$ *IEEE symposium on ultrasonics* (IEEE) pp 435–438
[27] Ugarak F, Iglesias Martínez J A, Mosset A and Laude V 2023 *Journal of Applied Physics* **134**
[28] Leisure R G, Hsu D K and Seiber B A 1973 *Journal of Applied Physics* **44** 3394–3397
[29] Ruthenium 2025 in wikipedia, the free encyclopedia `https://en.wikipedia.org/wiki/Ruthenium` accessed: 2025-01-10
[30] Kundu T 2003 *Ultrasonic nondestructive evaluation: engineering and biological material characterization* (CRC press)
[31] Trzaskowska A, Mielcarek S and Sarkar J 2013 *Journal of Applied Physics* **114**
[32] Trzaskowska A, Mielcarek S, Graczykowski B and Stobiecki F 2012 *Journal of alloys and compounds* **517** 132–138
[33] Lopes Seeger R, La Spina L, Laude V, Millo F, Bartasyte A, Margueron S, Solignac A, de Loubens G, Thevenard L, Gourdon C, Chappert C and Devolder T 2024 *Phys. Rev. B* **109**(10) 104416
[34] Laude V and Wang Y F 2023 *Physical Review B* **107** 144301